Modeling and Control of Inductive Power Transfer System Supplied by Multiphase Phase-Controlled Inverter

Qijun Deng, Ziyi Wang, Cheng Chen, *Student Member, IEEE*, Dariusz Czarkowski, *Member, IEEE*, Marian K. Kazimierczuk, *Fellow, IEEE*, Hong Zhou, *Member, IEEE*, and Wenshan Hu, *Member, IEEE*

***Abstract*—A multiphase inverter with phase-shifted control is proposed for the inductive power transfer (IPT) of electric vehicles where the charging voltage can be regulated by adjusting the angle among the inverter phases. An equivalent circuit model is developed and linearized to analyze the system dynamic characteristics at its operating point. In terms of the high-order model, a balanced model reduction method is used to remove the fast modes that are outside the desired system bandwidth and insignificant to controller design. In addition, the model is discretized and the communication delay of the feedback loop is considered in the discretized model. Based on this model, the parameters of a PI controller are designed to achieve the expected performance indexes. A 6.5 kW S-S compensation IPT system prototype with constant voltage control is built and tested to verify the control performance. The experimental results show that the charging voltage can be maintained constant within 6 ms and has no overshoot under disturbances, which verifies that the closed-loop system with PI controller operates properly and efficiently for IPT. Besides, the measured transmission efficiency of the system at a receiving power of 6.5 kW is 95.1%.**

***Index Terms*—Constant voltage control, inductive power transfer (IPT), phase-shift controlled inverter, PI controller, small-signal modeling.**

Manuscript received June 5, 2018; revised September 26, 2018 and November 18, 2018; accepted December 7, 2018. Date of publication December 14, 2018; date of current version June 10, 2019. This work was supported in part by the National Natural Science Foundation of China under Grant 51677139 and in part by the Basic Research Project of Shenzhen Science and Technology Commission under Grant JCYJ2017081811280674. Recommended for publication by Associate Editor J. M. R. Davila. *(Corresponding author: Cheng Chen.)*

Q. Deng is with the School of Electrical Engineering and Automation, Wuhan University, Wuhan 430072, China and also with Shenzhen Research Institute, Wuhan University, Shenzhen 518057, China (e-mail:

To design a controller with satisfactory control performance, many modeling methods have been proposed for above charging power regulation methods. In [15] and [19], a state-space model of the bidirectional IPT system was developed. It is shown that this model can accurately describe the system and can be a valuable tool for both transient analysis and controller design. In [18] and [32], a technique based on extended describing functions is proposed for the WPT system of EVs charging. The model considers the input voltage, frequency, and duty cycle as variables to control the output voltage at a constant value, but lacks the phase-shift control. Alternatively, the small-signal modeling method is widely employed to establish a mathematical model for the IPT system [14], [30], [31]. A closed-loop controller, considering both the frequency and the phase-shift control to keep the output voltage constant is proposed in [30] and [31], but it is analyzed in the continuous time domain and does not take into consideration the digital control in the discrete domain. Also, the controllers proposed in these papers are directly designed based on high-order state-space models, which increases the difficulty of the controller design. Additionally, the most important thing is that the communication delay caused by the wireless modules in the control feedback loop is not considered in the controller design process.

The multiphase inverter with phase-shift control (or phase-control) is an encouraging alternative to the single-phase inverter of IPT system [33]. It shares advantages of higher output power and EMI reduction [23], [33]. Besides, it has the capacity to provide higher efficiency than half-bridge or full-bridge class-D topologies [33]. These are favorable to wireless charging of EVs. A three-phase phase-controlled inverter is introduced in [33] for EVs wireless charging. These three phases supply a single sending coil instead of three coils as [23]. The three-phase phase-controlled inverter regulates the output power by adjusting the phase-shift angle among phases under a constant operating frequency. However, it mainly focuses on how to meet the requirements of charging power and zero voltage switching (ZVS) operation under varying parameters, such as air gap or load resistance, but the modeling and controller design are not presented.

A multiphase phase-controlled resonant inverter is proposed in [34] and [35], where multiple identical switching-legs are connected in parallel using intercell transformers (ICT), which limit circulating currents among switching-legs. This kind of inverter greatly improves the output power capability so that it is very suitable for high-power applications, such as EVs [4].

Obtaining desired control performance is a key requirement while employing the multiphase phase-shift control inverter for IPT system. Compared with the existing literature above, this paper focuses on how to design a digital controller based on the mathematical model. The specific contributions of this paper are as follows:

1) A multiphase phase-controlled inverter is presented and applied to the IPT system. In order to analyze the system dynamic characteristics and design a controller, a common dynamic model including the proposed multiphase phase-controlled inverter and entire IPT system is obtained and deduced.
2) Due to the high order of the model, a balanced model reduction method is used to remove the fast modes that are outside the desired system bandwidth and insignificant to controller design.
3) Considering that the control feedback loop in the experiment is set up with the wireless modules, a few unit delays are added to the discrete model by using the Pade transform method. Also, the discrete domain analysis of the reduced model is conducted, which is more suitable for the digital control.
4) The phase margin, amplitude margin, settling time, and overshoot are all considered as the requirement performance indexes in the development of the controller. This is especially useful when the system is required to be tightly designed in terms of the expected settling time or overshoot.

This paper is organized as follows. In Section II, the multiphase phase-controlled inverter is analyzed and a common PI control strategy for S-S, S-P, P-S, and P-P compensated systems is proposed. Then, an S-S compensated equivalent circuit of IPT supplied by the multiphase phase-controlled inverter is modeled and analyzed in Section III. In addition, a digital PI controller is designed based on the results of the analysis. Section IV focuses on the analysis of ZVS operation and transmission efficiency of the system. Finally, a 6.5-kW IPT system prototype is built and the experimental results are provided in Section V. Conclusions are given in Section VI.

II. Analysis of the System and Control Strategy

A. Structure of the Proposed IPT System

The proposed IPT system supplied by a multiphase phase-controlled inverter is shown in Fig. 1. It consists of a multiphase phase-controlled inverter, magnetic resonance coupling parts, a full-bridge rectifier, and a battery equivalent series resistance (ESR). The multiphase phase-controlled inverter fed by a dc source V_I is composed of N half-bridge class-D switching legs connected in parallel with N cyclic cascade connection inductors (intercell transformer, ICT) $\mathrm{ICT}_1 - \mathrm{ICT}_N$. Each ICT has two windings that are connected as shown in Fig. 1. The cascade inductors act as impedances to allow for phase control and to suppress circulating currents among phases. The output voltages of the half-bridge class-D switching legs are $v_1, v_2, \ldots, v_N$, respectively. Moreover, the voltages between two adjacent switch legs have the same phase-shift angle φ_r. By changing φ_r, one can adjust the amplitude of the output voltage v_{ab} of the multiphase phase-controlled inverter. The resonant inductors L_p and L_s are two coaxial coils for transferring power. M is the mutual inductance between the sending coil and the receiving coil. R_p and R_s represent the equivalent resistors of two sides. R_b is the equivalent load resistance of the vehicle battery packs. The rectifier with a class-D full-bridge topology provides dc voltage V_o for the filter capacitor C_f and the battery load R_b.v_{cd} is the input voltage of the rectifier. Two wireless modules, a PI controller and a driving circuit, are adopted to form a closed control-loop to regulate the charging voltage V_o.

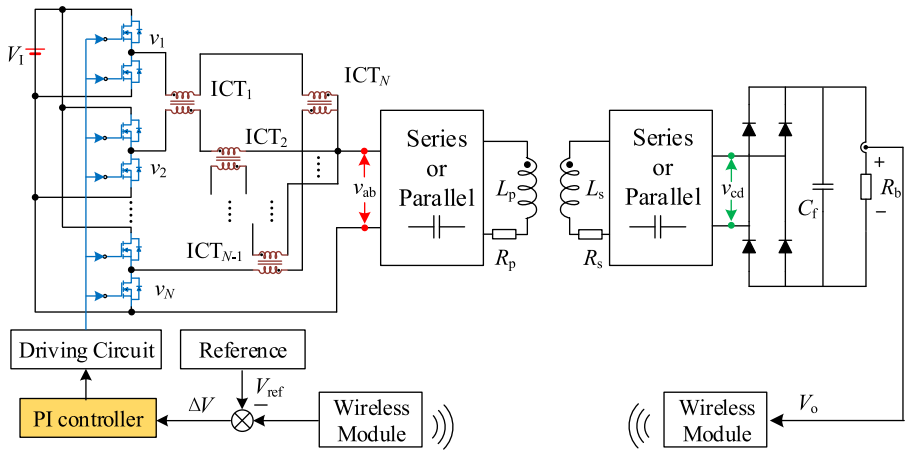

Fig. 1. Scheme of the IPT system driven by a multiphase phase-controlled inverter.

B. Analysis of the Multiphase Phase-Controlled Inverter

Since only the fundamental component current with the frequency ω_s close to the resonant frequency of the circuit can flow through the *LC* resonance circuit, the dc and higher harmonic components in $v_1, v_2, \ldots, v_N$ can be ignored. Therefore, the square wave voltage sources of the kth phase can be replaced by their fundamental components as following [34]:

$$v_k = V_m \cos\left(\omega_s t + \frac{2k\varphi_n}{N} - \frac{(N-1)\,\varphi_n}{N}\right) \tag{1}$$

where N is the number of the phase, k is from 1 to N, and φ_n is the normalized phase shift in a range from 0 to π that gives full control range. Under a duty cycle of 0.5 for each inverter lag, the voltage amplitude is $V_m = 2V_I/\pi$. The voltages across the primary compensation network caused by the sinusoidal voltage sources v_k separately, i.e., with the other voltage source shorted, are expressed as

$$v_{\mathrm{abk}} = \frac{v_k Z_{\mathrm{in}}}{Z_{\mathrm{ICT}} + NZ_{\mathrm{in}}} \qquad (k = 1, 2, ..., N) \tag{2}$$

where Z_{ICT} is the impedance of each phase of the phase-controlled inverter and Z_{in} is the load impedance of the phase-controlled inverter. Fig. 2 shows the relationship between the square wave voltage sources $v_1, v_2, \ldots, v_N$ and the fundamental component of v_{ab}. The step width φ_r of the voltage curve v_z represents the phase-shift angle between two adjacent switch legs, which can be expressed as

$$\varphi_r = \frac{2\varphi_n}{N}. \tag{3}$$

Using the principle of superposition, one can obtain the voltage across the primary compensation network as

$$v_{ab} = \sum_{k=0}^{N-1} \frac{v_k Z_{\mathrm{in}}}{Z_{\mathrm{ICT}} + NZ_{\mathrm{in}}} = \frac{2V_I \sin\varphi_n}{N\pi \sin\frac{\varphi_n}{N}} \sin(\omega_s t). \tag{4}$$

Hence, the dc-to-ac voltage transfer function of the phase-controlled inverter is

$$M_{ab} = \frac{|v_{ab}|}{V_I} = \frac{2\sin\varphi_n}{N\pi \sin\frac{\varphi_n}{N}}. \tag{5}$$

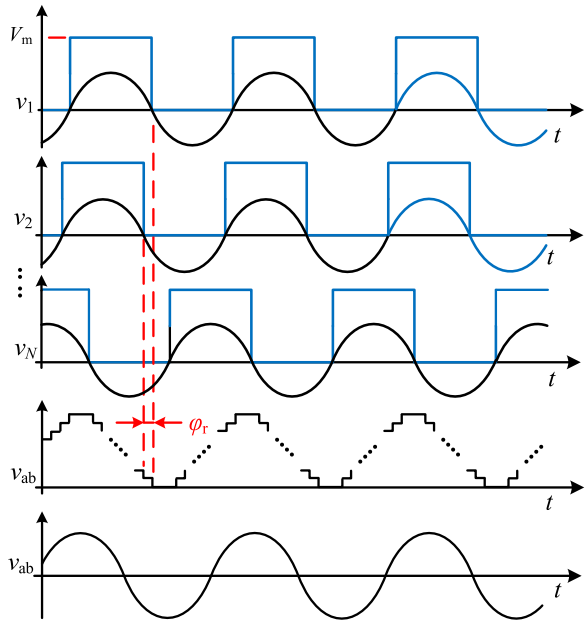

Fig. 2. Waveforms of output voltage and fundamental component for N phases and the resulting one under a phase-shift angle of φ_r.

According to (5), Fig. 3 illustrates M_{ab} as a function of the normalized phase-shift angle φ_n for a different number of phases N. It can be seen that M_{ab} for different values of N are decreasing from 0.64 to 0 when φ_n is increasing from 0° to 180°. In other words, the output voltage of the multiphase phase-controlled inverter decreases with the increasing of the normalized phase-shift angle φ_n.

C. Control Scheme

Based on the analysis in the previous section, a common digital PI control strategy for S-S, S-P, P-S, and P-P topologies is proposed to implement phase shift control. Fig. 4 shows the detailed flowchart of the control strategy. It consists of preset reference voltage, PI controller, multiphase phase-controlled inverter, IPT system, zero-order holder, and wireless communication. First, the charging voltage is sampled and transmitted by wireless communication module to the processor at the

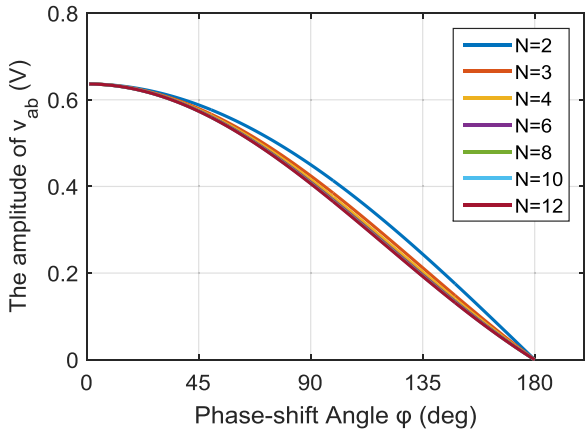

Fig. 3. Magnitude of the dc–ac transfer function of the phase-controlled inverter M_{ab} as a function of the normalized phase-shift angle φ_n for different phase number of N.

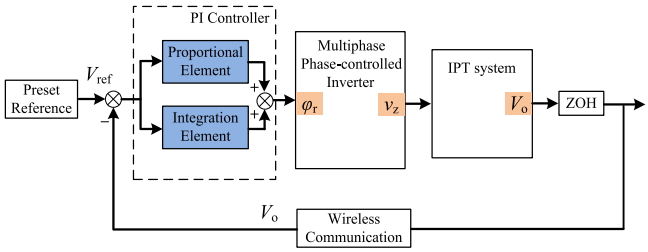

Fig. 4. Detailed flowchart of the proposed control Scheme.

sending side. Then, by comparing with the preset reference, the voltage difference is converted by the PI controller into a new phase shift angle of the multiphase phase-controlled inverter. Finally, the IPT system is activated by the inverter and the charging voltage is controlled.

S-S topology is widely used for EVs charging as the compensation capacitors are independent of the coupling coefficient and load [36]. Therefore, this paper will focus on the modeling, analyzing, and digital controller design of the S-S topology while ignoring other compensation topologies (i.e., S-S, S-P, P-S, and P-P).

III. Dynamic Modeling and Controller Design

A. Simplification of the S-S Compensated IPT System

The equivalent of the IPT circuit is necessary for developing a dynamic model and designing a controller. Based on the circuit theory, the magnetic coupling between coils can be expressed as

$$v_{ep} = M\frac{di_p}{dt}, \quad v_{es} = M\frac{di_s}{dt} \tag{6}$$

where i_p and i_s are currents at each side through corresponding resonant inductor, respectively. The ac state variable i_p and v_p (the voltage of the resonant capacitor at the primary side) can be decomposed using the *d-q* decomposition method [11] as

$$\begin{aligned} i_p &= I_{pd}\sin(\omega_s t) + I_{pq}\cos(\omega_s t) \\ v_p &= V_{pd}\sin(\omega_s t) + V_{pq}\cos(\omega_s t) \end{aligned} \tag{7}$$

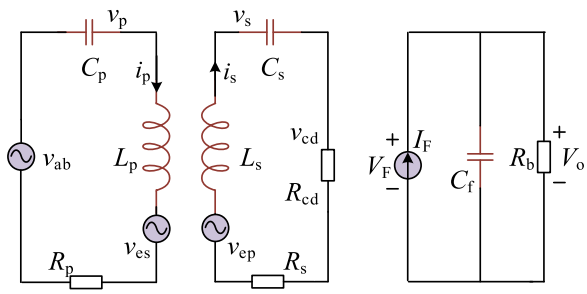

Fig. 5. Equivalent circuit of the S-S compensated IPT system.

where I_{pd}, I_{pq}, V_{pd}, and V_{pd} are dc components of i_p and v_p mapping on two orthogonal coordinate axes, d-axis and q-axis, respectively. With the same method depicted by (7), the ac state variables i_s and v_s (the voltage of the resonant capacitor at the secondary side) can also be decomposed and expressed by dc variables I_{sd}, I_{sq}, V_{sd}, and V_{sq}, respectively.

For the full-bridge rectifier, the ac and dc components of the voltage and current can be respectively written as

$$\begin{aligned} v_{cd} &= \text{sign}(i_s)\cdot V_F = \frac{4}{\pi}\frac{i_s\cdot V_F}{|i_s|} \\ &= \frac{4}{\pi}\frac{I_{sd}\cdot V_o}{\sqrt{I_{sd}^2+I_{sq}^2}}\cdot\sin(\omega_s t) + \frac{4}{\pi}\frac{I_{sq}\cdot V_o}{\sqrt{I_{sd}^2+I_{sq}^2}}\cdot\cos(\omega_s t) \end{aligned} \tag{8}$$

$$I_F = \frac{2}{\pi}\sqrt{I_{sd}^2+I_{sq}^2} \tag{9}$$

where v_{cd} and i_s are the ac input voltage and current of the rectifier; V_F and I_F are the dc output voltage and current of the rectifier [30], [31]. The ESR R_{cd} of the full-bridge rectifier can be replaced by [33]

$$R_{cd} = 8R_b/\pi^2. \tag{10}$$

Considering (6) and (8) through (10), the main circuit of the S-S compensated IPT system in Fig. 1 can be simplified to an equivalent circuit as shown in Fig. 5.

B. Establishment of Dynamic Equations

Applying Kirchhoff's voltage law and Kirchhoff's current law, the dynamic equations of the equivalent circuit are as follows:

$$\begin{aligned} v_{ab} &= i_p R_p + v_p + L_P\frac{di_p}{dt} - v_{es} \\ i_p &= C_p\frac{dv_p}{dt} \\ v_{ep} &= L_s\frac{di_s}{dt} + v_{cd} + i_s R_s + v_s \\ i_s &= C_s\frac{dv_s}{dt} \\ I_F &= C_f\frac{dV_o}{dt} + \frac{V_o}{R_b}. \end{aligned} \tag{11}$$

Substitution (6) through (10) into (11) leads to the separation of *d-q* components by

$$\begin{aligned}
\frac{d}{dt}(I_{pd}) &= \omega_s I_{pq} + A_2 \frac{2V_I}{3\pi} \frac{\sin\varphi_n}{\sin\frac{\varphi_n}{N}} \\
&\quad - A_2 R_p I_{pd} - A_2 V_{pd} - A_3 (A_{11} I_{sd} + V_{sd}) \\
&\quad - A_3 R_s I_{sd} \\
\frac{d}{dt}(I_{pq}) &= -\omega_s I_{pd} - A_2 R_p I_{pq} - A_2 V_{pq} \\
&\quad - A_3 (A_{11} I_{sq} + V_{sq}) - A_3 R_s I_{sq} \qquad (12a) \\
\frac{d}{dt}(V_{pd}) &= \frac{1}{C_p} I_{pd} + \omega_s V_{pq} \\
\frac{d}{dt}(V_{pq}) &= \frac{1}{C_p} I_{pq} - \omega_s V_{pd} \qquad (12b) \\
\frac{d}{dt}(I_{sd}) &= \omega_s I_{sq} + A_3 \frac{2V_I}{3\pi} \frac{\sin\varphi_n}{\sin\frac{\varphi_n}{N}} - A_3 R_p I_{pd} \\
&\quad - A_3 V_{pd} - A_1 (A_{11} I_{sd} + V_{sd}) - A_1 R_s I_{sd} \\
\frac{d}{dt}(I_{sq}) &= -\omega_s I_{sd} - A_3 R_p I_{pq} - A_3 V_{pq} \\
&\quad - A_1 (A_{11} I_{sq} + V_{sq}) - A_1 R_s I_{sq} \qquad (12c) \\
\frac{d}{dt}(V_{sd}) &= \frac{1}{C_s} I_{sd} + \omega_s V_{sq} \\
\frac{d}{dt}(V_{sq}) &= \frac{1}{C_s} I_{sq} - \omega_s V_{sd} \qquad (12d) \\
\frac{d}{dt}(V_o) &= \frac{2}{\pi C_f} \sqrt{I_{sd}^2 + I_{sq}^2} - \frac{V_o}{C_f R_b} \qquad (12e)
\end{aligned}$$

where the variables A_1 through A_{11} are listed in the Appendix.

This is a set of nine nonlinear differential equations. In order to analyze the dynamic characteristics of the system, these nonlinear differential equations need to be linearized around an expected operating point.

TABLE I
PARAMETERS OF THE IPT SYSTEM

Symbol	Parameter Explanation	Value
$V_{\rm I}$	DC Voltage Input of the Inverter	350 V
$f_{\rm s}$	Operation Frequency	86 kHz
$R_{\rm p}$	Equivalent Series Resistance at Primary Side	0.04 Ω
$R_{\rm s}$	Equivalent Series Resistance at Secondary Side	0.04 Ω
M	Mutual inductance between two coils	7.33 μH
$L_{\rm p}$	Resonant Inductance on Primary Side	34 μH
$L_{\rm s}$	Resonant Inductance on Secondary Side	34 μH
$C_{\rm p}$	Resonant Capacitance on Primary Side	117 nF
$C_{\rm s}$	Resonant Capacitance on Secondary Side	117 nF
$C_{\rm f}$	Filtering Capacitance	300 μF
$r_{\rm MOS}$	ESR of the MOSFET	0.04 Ω
$r_{\rm ICT}$	ESR's of intercell transformer windings	0.03 Ω
L_{mag}	Magnetizing inductance of intercell transformer	35 μH
L_{leak}	Leakage inductance of intercell transformer	3.5 μH
$t_{\rm r}$	Raising time of the MOSFET	28 ns
$t_{\rm f}$	Falling time of the MOSFET	8 ns
$r_{\rm Cf}$	Parasitic resistance of the rectifier filter capacitor	0.005 Ω
$V_{\rm Cf}$	Forward voltage of the rectifier diodes	0.7 V
$R_{\rm F}$	ESR of the rectifier diodes	0.005 Ω
$R_{\rm b}$	Resistance of the Load	5 Ω

C. Small-Signal Modeling and Reduction

The above nonlinear differential equations can be expressed in the state-space form as follows:

$$\begin{cases} \dot{X} = AX + BU \\ Y = CX \end{cases} \qquad (13)$$

where *A*, *B*, and *C* are the partial derivative matrices of (12), and given by (14). The state variable X, input vector U, and the output vector Y are expressed by $X = [I_{pd}, I_{pq}, V_{pd}, V_{pq}, I_{sd}, I_{sq}, V_{sd}, V_{sq}, V_o]^T$, $U = \varphi_n$ and $Y = V_o$, where V_o is the charging voltage. By linearization around the operating point, one can get a small-signal model of (13). In this paper, a three-phase phase-controlled inverter, namely, $N = 3$, is selected as an example. In order to maintain a constant charging voltage, the preset reference voltage is set to be 125 V. Using the main parameters of the system in Table I while setting the

$$A = \begin{bmatrix}
-A_2R_p & \omega_s & -A_2 & 0 & -A_3A_4 & A_3A_8 & -A_3 & 0 & -A_3A_6 \\
-\omega_s & -A_2R_p & 0 & -A_1 & A_3A_8 & -A_3A_5 & 0 & -A_3 & -A_3A_7 \\
1/C_p & 0 & 0 & \omega_s & 0 & 0 & 0 & 0 & 0 \\
0 & 1/C_p & -\omega_s & 0 & 0 & 0 & 0 & 0 & 0 \\
-A_3R_p & 0 & -A_3 & 0 & -A_2A_4 & \omega_s + A_2A_8 & -A_2 & 0 & -A_2A_6 \\
0 & -A_3R_p & 0 & -A_3 & -\omega_s + A_2A_8 & -A_2A_5 & 0 & -A_2 & -A_2A_7 \\
0 & 0 & 0 & 0 & 1/C_s & 0 & 0 & \omega & 0 \\
0 & 0 & 0 & 0 & 0 & 1/C_s & -\omega_s & 0 & 0 \\
0 & 0 & 0 & 0 & A_6/(2C_f) & A_7/(2C_f) & 0 & 0 & -1/(C_fR_b)
\end{bmatrix} \qquad (14a)$$

$$B = \begin{bmatrix} -A_2A_9 & 0 & 0 & 0 & -A_3A_9 & 0 & 0 & 0 & 0 \end{bmatrix}^T \qquad (14b)$$

$$C = \begin{bmatrix} 0 & 0 & 0 & 0 & 0 & 0 & 0 & 0 & 1 \end{bmatrix} \qquad (14c)$$

derivatives given in (12) to be zero, one can obtain the operating point for the S-S compensated IPT system as

$$X_o = [45.83\ -13.64\ -215.78\ -724.97\ 29.42\ 25.99\ 411.09\ -465.41\ 124.96]^T. \tag{15}$$

Substitution (15) and Table I into (14) produces the small-signal model

$$\begin{cases} \dot{X}_o = A_o X_o + B_o U_o \\ Y_o = C_o X_o. \end{cases} \tag{16}$$

This ninth-order linearized model expressed by (16), however, incurs great difficulty in terms of model analysis and digital controller design due to its high order and continuous time domain form. Thus, the model reduction and discretization is essential. In this section, a balanced model reduction method is used to remove the fast modes that are outside the desired system bandwidth and insignificant to controller design. The operation principle of the reduction method is briefly explained as follows.

First, one of the state-space realizations, namely, the balanced realization and Gramian matrix, is employed to describe the controllability and observability of the linearized model. According to (16), the Gramian matrix can be presented as

$$G = [1.0916\ 0.0556\ 0.0119\ 0.0113\ 5.30e-3\ 7.48e-4\ 7.40e-4\ 4.24e-4\ 4.13e-4]^T. \tag{17}$$

Each element in the Gramian matrix indicates the degree of controllability and observability of the corresponding mode, in other words, the bigger the element, the stronger the controllability and observability.

Second, the linearized model is reduced to a lower order one by removing the small elements in (17). In this application, the model (16) can be reduced by truncating the last five elements in (17). Keeping the first four rows and columns, the balanced matrix A_b, B_b, and C_b are given by

$$\begin{aligned} A_b &= \begin{bmatrix} -1.27e3 & 2.94e3 & -983.7 & 103.3 \\ -2.94e3 & -3.02e4 & 2.74e4 & -1.84e3 \\ -983.7 & -2.74e4 & -1.80e4 & -7.77e4 \\ -103.3 & -1.84e3 & -7.77e4 & -199.8 \end{bmatrix} \\ B_b &= \begin{bmatrix} -52.58\ 58.0\ 20.65\ 2.12 \end{bmatrix}^T \\ C_b &= \begin{bmatrix} -52.58\ 58.0\ -20.65\ 2.12 \end{bmatrix}. \end{aligned} \tag{18}$$

Finally, the reduced open-loop transfer function model of the system, where the normalized phase-shift angle φ_n is the input and charging voltage V_o is the output, is given as

$$G_p(s) = \frac{Y(s)}{U(s)} = \frac{-177.3s^3 + 3.9e7s^2 - 2.7e11s + 6.1e17}{s^4 + 5e4s^3 + 7.4e9s^2 + 2e14s + 3e17}. \tag{19}$$

Using MATLAB, the Bode diagrams of this reduced fourth-order model and the original model are drawn in Fig. 6. It can be seen that both models have the same frequency characteristics within the angular frequency of 2.1×10^5 rd/s, which proves that the reduction of the model is accurate.

What is worth mentioning, although an S-S compensated IPT system with a three-phase phase-controlled inverter is mainly concerned in this paper, the proposed modeling and reducing method can also be applied to an S-P, P-S, or P-P compensated system with a multiphase phase-controlled inverter. Again, the constant current charging control can be applied equally by selecting a corresponding output for the dynamic model (13).

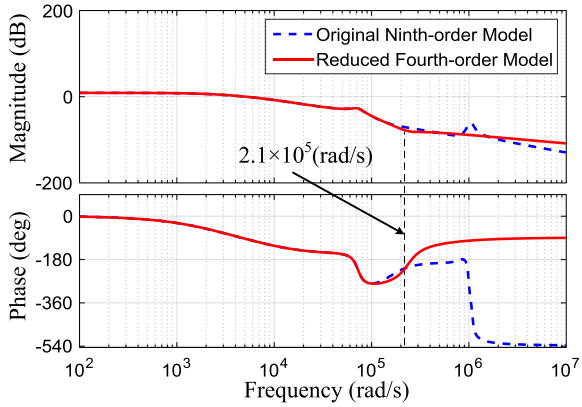

Fig. 6. Bode diagram of the reduced fourth-order model and the original ninth-order model.

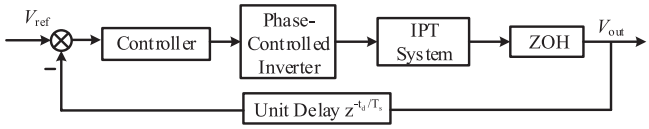

Fig. 7. Block diagram of the closed-loop system with communication delay.

D. Model Discretization and Digitized Controller Design

According to the proposed digital control strategy depicted by Fig. 4, the reduced model (19) needs to be discretized and analyzed in the discrete-time domain. A sampling rate $T_s = 0.05$ ms is selected, which takes into account the operating frequency, the closed-loop bandwidth requirement, and the antialias requirement of the sampling circuit. Using Euler's method and considering the zero-order hold delay, the transfer function of the reduced model can be digitized as

$$G_{pz}(z) = \frac{0.061z^3 + 0.10z^2 + 0.063z + 0.016}{z^4 - 0.46z^3 - 0.24z^2 - 0.26z + 0.083}. \tag{20}$$

In a practical IPT system, it takes some time for the wireless module to transmit the charging voltage data from the secondary side to the primary side. If this time delay is comparable to the sampling period, its influence on the system must also be considered. In this paper, the wireless communication is set up with two nRF24L01 modules, which transmit 8 B at a time with a 2 Mb/s baud rate. According to the specification of this kind of wireless module, the required delay to send a packet of data and receive the response signal is $t_d = 0.37$ ms, which is much bigger than the sampling period. Therefore, a few unit delays, as shown in Fig. 7, are added between the wireless module and the controller input. Also, to overcome the higher order problem, the Pade transform method is used. The discretized model with

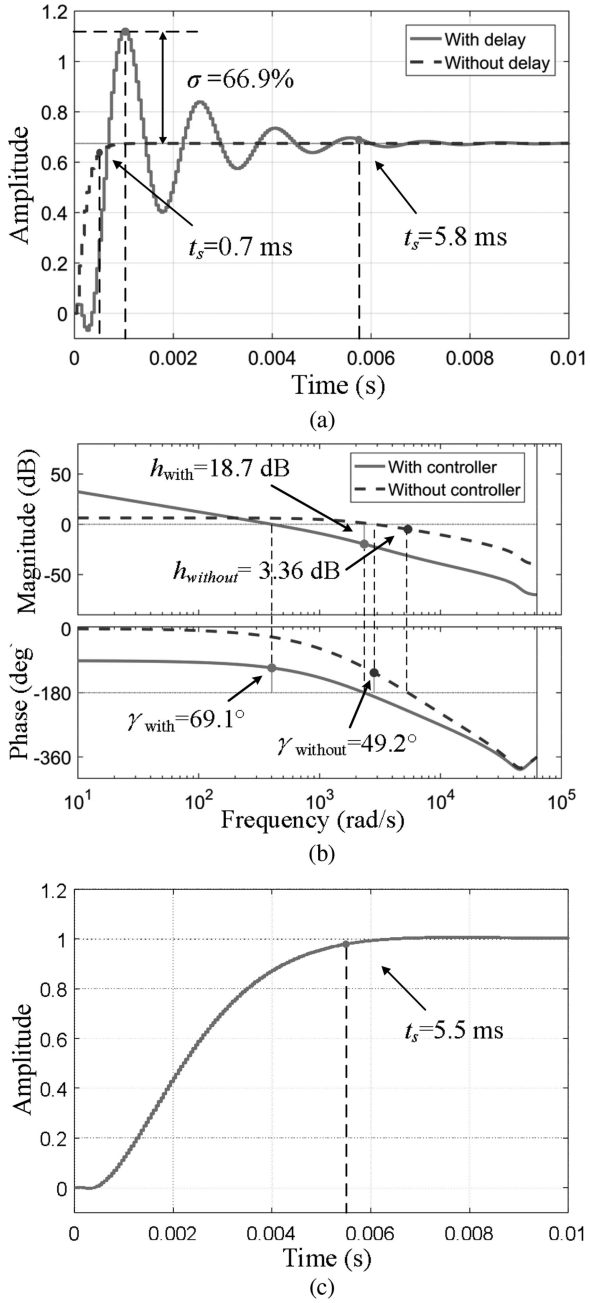

Fig. 8. Dynamic analysis of the obtained models. (a) Unit step response of the feedback digitized model with and without delay. (b) Stability phase and margin characteristics of model (21) with the designed controller. (c) Unit step response of model (21) with the designed controller.

the delay can be expressed as

$$G_{\mathrm{pzd}}(z) = \frac{0.04z^5 - 0.06z^4 - 0.01z^3 + 0.02z^2 + 0.05z + 0.01}{z^6 - 1.75z^5 + 0.80z^4 - 0.15z^3 + 0.32z^2 - 0.22z + 0.04}. \tag{21}$$

Fig. 8(a) shows the unit step response of the feedback digitized model with and without delay. Compared to the curve without delay, one can see that the communication delay makes the dynamic performance of the system worse. The settling time increased from 0.7 to 5.8 ms, and the overshoot of the model that is not advocated in many applications is increased from 0% to 66.9%. Thus, a digital controller is necessary to control the output voltage.

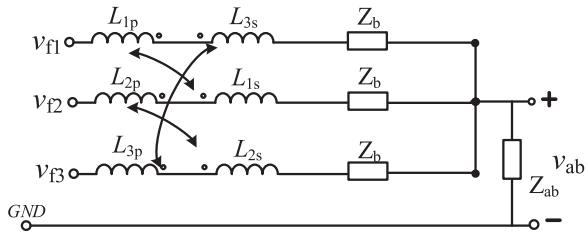

Fig. 9. Equivalent circuit of three-phase phase-controlled inverter.

The digitized PI controller has the following form:

$$P(Z) = K_p\left(1 + \frac{1}{T_i}\frac{T_s}{2}\frac{Z+1}{Z-1}\right) \tag{22}$$

where K_p and T_i are the proportional coefficient and the integral time, respectively. In this section, in order to obtain the ability to respond fast and avoid overcurrent during the charging process, the requirement performances of the system, such as the settling time and overshoot are set to be 5.5 ms and 0%, respectively. This is because the limitation of oscillation takes precedence over the settling time for the sake of the charging safety. After several adjusting of K_p and T_i, the final parameters $K_p = 0.03$ and $T_i = 1.2 \times 10^{-4}$ are employed.

Fig. 8(b) depicts the stability phase and margin characteristics of the reduced model with and without the designed controller. One can see from the phase and amplitude margin that the control-loop is stable. In addition, the amplitude margin of the control-loop with the designed controller is optimized from 3.36 to 18.7 dB and the phase margin is optimized from 49.2° to 69.1°, which indicates that the system with PI controller is more robust. The unity-step response of the closed-loop system with the designed controller is shown in Fig. 8(c). One can obtain from the response curves that the unity feedback system responds to a step change with the settling time $t_s = 5.5$ ms and the overshoot $\sigma\% = 0\%$, which meet the expectations.

IV. ZVS and Efficiency Analysis

A. ZVS for Three-Phase Phase-Controlled Inverter

For the three-phase phase-controlled inverter where each phase connected via three cyclic cascade connection inductors, its equivalent circuit can be depicted by Fig. 9, where Z_{in} is the equivalent input impedance of the inverter. According to (1) and (2) in Section II, the voltage $v_{\mathrm{ab}k}$ $(k = 1, 2, 3)$ of each phase can be obtained. Also, one can obtain the currents i_k through solving following equations:

$$\begin{cases} \sum_{k=1}^{3} i_k = \dfrac{v_{ab}}{Z_{\mathrm{in}}} \\ i_k - i_{k+1} = \dfrac{v_{abk} - v_{abk+1}}{j\omega_s L_{\mathrm{mag}}} \end{cases} \tag{23}$$

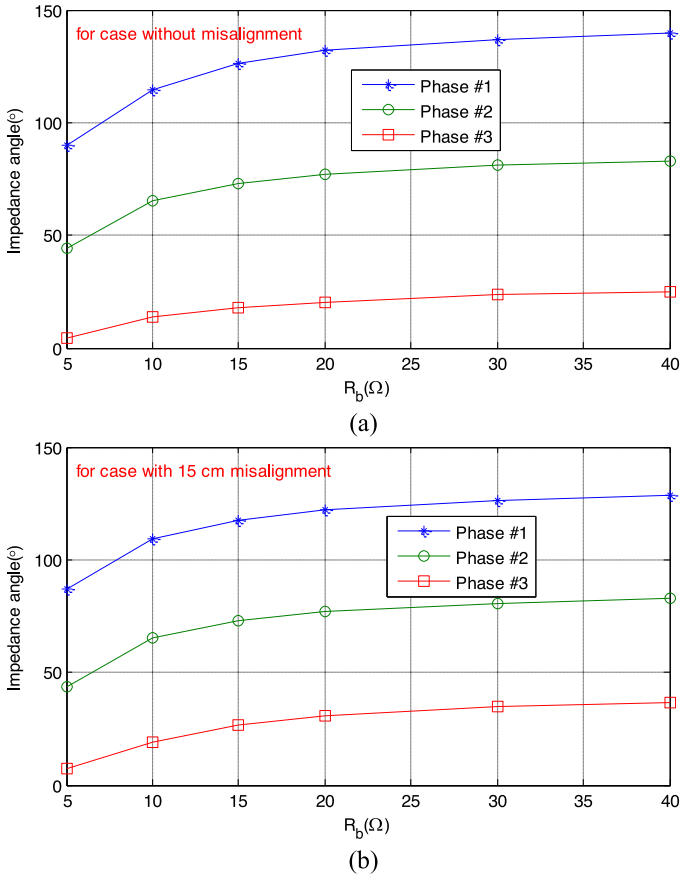

Fig. 10. Impedance angles versus load resistance for cases (a) without misalignment and (b) with 15 cm horizontal misalignment.

where L_{mag} is the mutual inductance between two windings of each ICT. Therefore, the impedance angles of each phase can be expressed as

$$\theta_k = \arctan\left(\mathrm{imag}\left(\frac{v_k}{i_k}\right), \mathrm{real}\left(\frac{v_k}{i_k}\right)\right). \tag{24}$$

Fig. 10 shows the impedance angles versus load resistance with or without 15 cm horizontal misalignment. As can be seen that the required phase angle φ_r for the load range of $5, 10, 15, 20, 30$, and $40\,\Omega$ under are $52°, 57°, 62°, 65°, 66°$, and $67°$, respectively. With the same method, impedance angles under 15 cm misalignment is obtained and depicted in Fig. 10(b). It can be seen that impedance angles are all higher than zero, which means ZVS condition still can be maintained.

B. Efficiency Analysis

The transmission efficiency can be calculated by

$$\eta = \frac{P_{\mathrm{load}}}{P_{\mathrm{load}} + P_{\mathrm{Ploss}} + P_{\mathrm{Sloss}}} \tag{25}$$

where P_{load} is the power obtained from the battery load, P_{Ploss} is the overall loss of the primary side, which consists of the primary conduction loss P_{pconduct} and primary switching loss P_{pssw}, and P_{Sloss} is the overall loss of the secondary side [33].

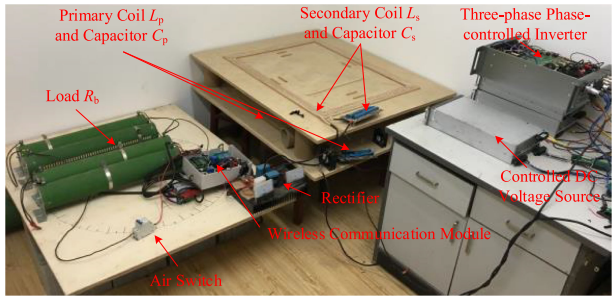

Fig. 11. Physical experimental setup of the S-S compensated IPT prototype.

The power obtained from the load is

$$P_{\mathrm{load}} = \frac{4I_s^2 R_b}{\pi^2} \tag{26}$$

where I_s is the magnitude of i_s. The primary conduction loss P_{pconduct} and primary switching loss P_{pssw} can be expressed as

$$P_{\mathrm{pconduct}} = (r_{\mathrm{MOS}} + r_{\mathrm{ICT}}) \sum_{i=1}^{3} I_i^2 + \frac{I_p^2 R_p}{2}$$

$$P_{\mathrm{pssw}} = \frac{\omega_s (t_r/3 + t_f/2) \sum_{i=1}^{3} I_i \sin\theta_i}{2\pi} \tag{27}$$

where r_{MOS} and r_{ICT} are the ESR of the MOSFET and ICT. I_i and θ_i $(\mathrm{i} = 1, 2, 3)$ are the magnitudes of the current and the phase angle for each phase. R_p is the ESR of the primary resonant capacitor and inductor. t_r and t_f are the rising time and falling time of the MOSFET, respectively.

The overall loss of the secondary side is

$$P_{\mathrm{Sloss}} = \sqrt{2} V_{Cf} I_s + \frac{\left(2R_F + R_s + r_{Cf}\left(\pi^2/4 - 1\right)\right) I_s^2}{2} \tag{28}$$

where R_F and r_{Cf} are the ESR of the rectifier diodes and filter capacitor, V_{Cf} is the forward voltage of the secondary side rectifier diodes, and R_s is the ESR of the secondary resonant capacitor and inductor.

V. Experimental Results

A. Prototype of the IPT System

An IPT prototype was built for experiments as shown in Fig. 11 whose parameters are listed in Table I. This prototype is composed of a multiphase phase-controlled inverter, a resonant wireless bank consisting of two inductor coils, a simple class-D full-bridge rectifier, and an *RC* circuit used as a filter. The wireless communication for the charging voltage data was set up with two nRF24L01 modules. Six IPW65R041CFD MOSFETs were used for the three-phase phase-controlled inverter. The controller was implemented with two MCUs, namely, an FPGA (XC6SLX9-3TQG144I) and an ARM (STM32F407VGT). The FPGA, whose counting frequency is 199.5 MHz, provides functions of counters and timers for MOSFETs switching signals. For example, an FPGA timer whose counting range is 0 through 2319 CLKs yields a frequency of 86 kHz. The ARM was used to calculate the phase-shift angle, while the FPGA generated driving signals for MOSFETs according to the phase-shift commands

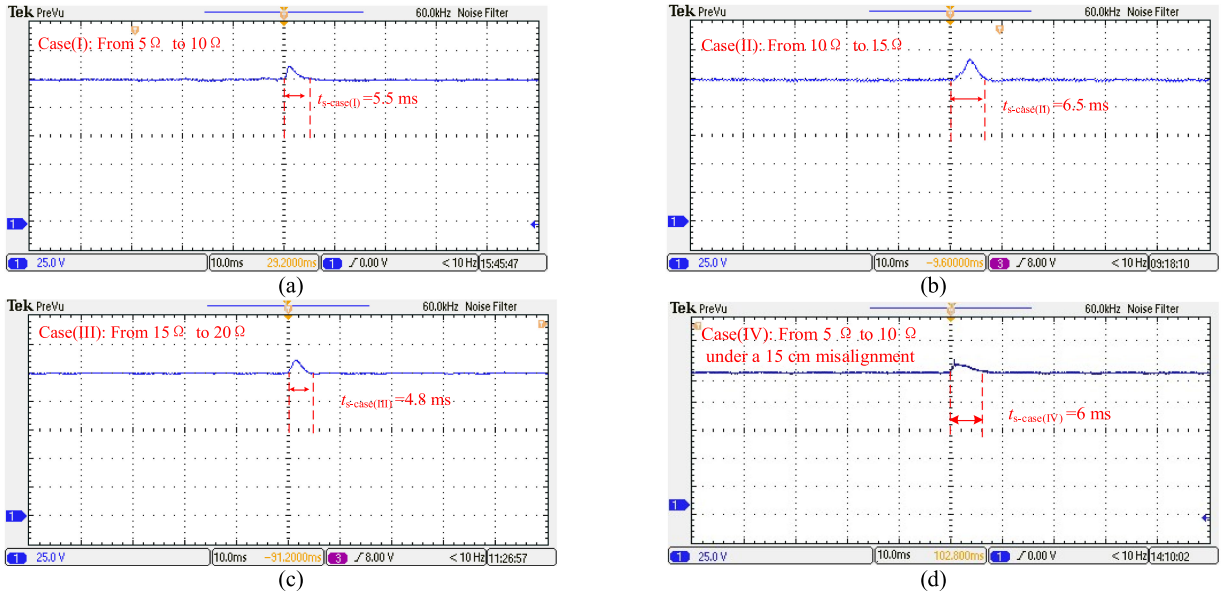

Fig. 12. Output voltage waveforms at a reference of 125 V with load resistance change. (a) From 5 to 10 Ω. (b) From 10 to 15 Ω. (c) From 15 to 20 Ω. (d) From 5 to 10 Ω under a 15 cm misalignment.

from the ARM. Taking a 18° phase-shift (i.e., 232 CLKs under 199.5 MHz FPGA counting frequency together with 86 kHz operating frequency) as an example, the switching time for corresponding MOSFETs of three phases can be 0, 232, and 464 CLKs, respectively.

The dimensions of the two coaxial coils were the same, whose rectangular outer ring was 90 cm × 70 cm. The distance between the coils was 20 cm. Each coil was built with four turns of Liz-wire. The diameter of the Litz-wire consisting of 2000 isolated strands was 6 mm and the diameter of each strand was 0.1 mm. At the secondary side, a class-D full-bridge rectifier was constructed using four VS-UFB280FA40 diodes.

In a typical three-stage charging process, namely, constant-current, constant-voltage, and ting-current charging, the equivalent load expressed by the charging voltage divided by the current is increasing during the charging process. In order to verify the robust ability of the controller during the whole charging process [33], [37], three cases of step-changing loads were employed for experiments, namely, from 5 to 10 Ω, from 10 to 15 Ω, and from 15 to 20 Ω. Several 10 Ω resistors were connected in parallel or series with an air switch. By controlling the opening or closing the switch, the load resistance can be changed conveniently.

B. Experiment Under Disturbances

Experiments of the load resistance disturbance were conducted with a fixed reference voltage 125 V. The charging voltages of the load resistance were captured by an oscilloscope as shown in Fig. 12(a)–(c). Besides, experiment for the case of 15 cm misalignment was also conducted and the voltages was captured in Fig. 12(d) to test the controller performance under coil misalignment. Although the output voltages rise rapidly as load changes in Cases (I)–(IV), they gradually return to the reference of 125 V with the designed PI controller and no voltage overshoots are observed. The settling times and overshoots in Cases (I)–(IV) are measured and listed in Table II. It can be seen that the dynamic performance of Case (I) is fairly close to the results simulated with MATLAB in Fig. 8(b). In terms of Cases (II)–(IV), the settling times show a slight difference from the required one. This is because the operating point for Cases (II)–(IV) are further away from the point at which the controller is designed in terms of the load.

TABLE II
CONTROL PERFORMANCES AT DIFFERENT LOAD CASES

Case	Settling time	Overshoot
(I)	5.5 ms	0 %
(II)	6.5 ms	0 %
(III)	4.8 ms	0 %
(IV)	6 ms	0 %

In order to test the influence of the operating point deviation on the control performance, different resonant states were considered by adjusting the operation frequency. Fig. 13(a) and (b) depict the output voltage waveforms for load change from 5 to 10 Ω at various operation frequencies, namely, Case (V) f_s = 85 kHz, and Case (VI) f_s = 87 kHz, respectively. Comparing with Fig. 12(a), the voltages in Fig. 13(a) and (b) need more time to reach the reference value. Besides, two changes of reference voltage around the operating point, namely, Case (VII): from 125 to 100 V and Case (VIII): from 125 to 150 V, respectively, are considered in Fig. 13(c) and (d) with a fixed load of 5 Ω and a fixed operation frequency of 86 kHz. One can see that the voltage waveforms can reach the reference within 5.6 and 6 ms, respectively.

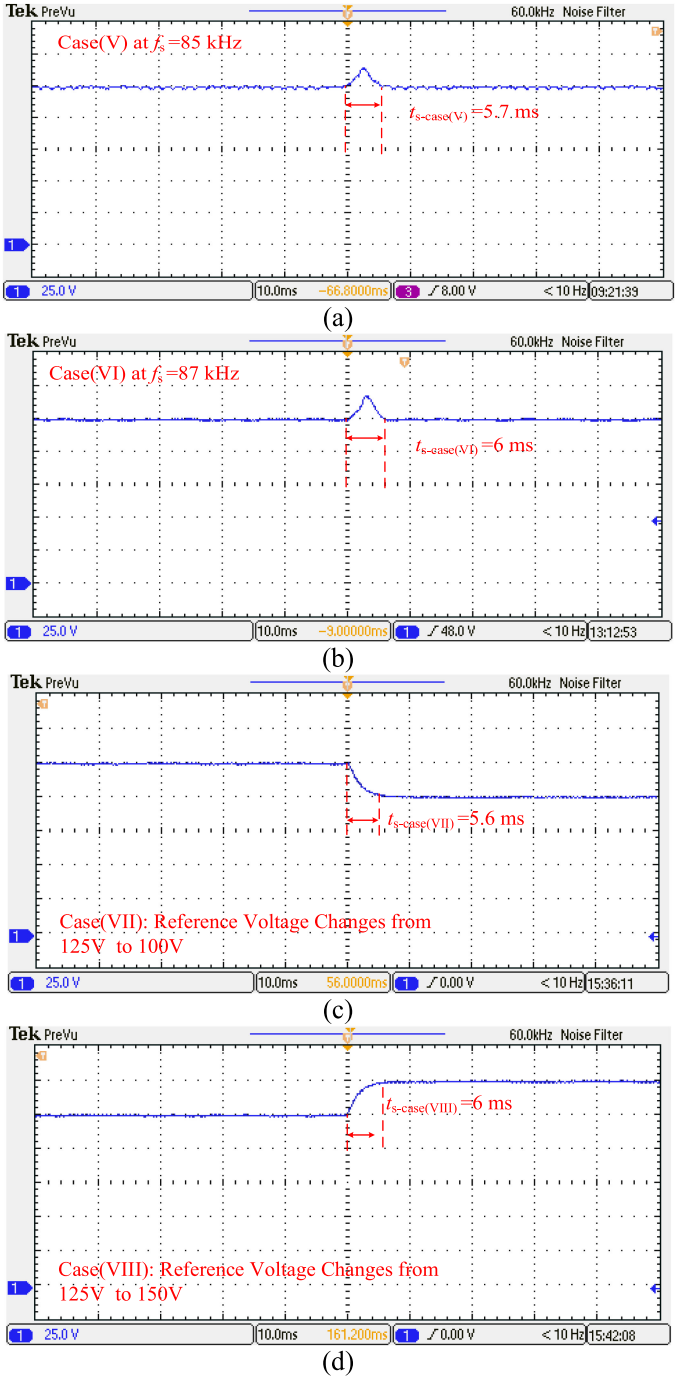

Fig. 13. Output voltage waveforms with a reference of 125 V under load change from 5 to 10 Ω at different resonant frequencies of (a) f_s = 85 kHz and (b) f_s = 87 kHz. Output voltage waveforms at 5 Ω resistance with reference voltage change of (c) from 125 to 100 V and (d) from 125 to 150 V.

From above experiments, some conclusions can be obtained as follows:

1) The output charging voltage is controllable during the entire charging process.
2) The dynamic performances of the system are affected by the load, operation frequency, and reference voltage.
3) Although affected by the change of the system operating point, the setting time is still very close to that at the operating point. This not only verifies that the established model reflects the dynamic characters of the system well, but also shows that the model can be applied to both the exact operating point and that near it.

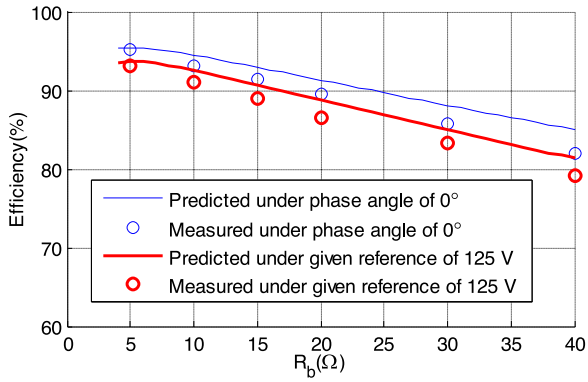

Fig. 14. Theoretical and experimental transmission efficiencies of the proposed IPT system versus the load resistance.

C. Efficiency and Inverter Output Analysis

With measured currents (i.e., I_S, I_P, I_1, I_2, and so on) and phase angles (i.e., θ_1 through θ_3), one can calculate the theoretical efficiency based on (25) and parameters listed in Table I. Fig. 14 shows the theoretical and experimental transmission efficiency of the proposed IPT system with the given reference voltage of 125 V. One can see that the experimental transmission efficiency matches the theoretical curve by the large. For the load resistance of 5 Ω, a maximum transmission efficiency of 93.9% is measured (output 125 V and 25 A at the load resistance, while input 350 V and 9.51 A for the inverter).

In practice, with the raising of the phase angle, the circulating currents among phases increase, which leads to higher loss. In order to check the highest efficiency without circulating current, another group of experiments were conducted when the PI controller is canceled deliberately (namely, the phase-shift angle is 0). System parameters are the same with Table I. The output voltage and current in the 5 Ω load resistance at the receiving side are 180.8 V and 36.16 A while the measured dc input current is 19.6 A at the sending side, respectively. Hence, the highest efficiency of the proposed topology is 95.3% at the power of 6.54 kW. In addition, the transmission efficiency gradually decreases with the load raising.

The waveforms of output voltage v_z and current i_p of the phase-controlled inverter under a reference voltage of 125 V and the load resistance $5, 10, 15, 20, 30$, and $40\,\Omega$, respectively, are captured with an oscilloscope and shown in Fig. 15(a)–(f). It can be seen from Fig. 13(a) that the phase-shift angle φ_r is about 52° when the load resistance is 5 Ω and the reference voltage is 125 V. When the load resistance increases to 10 Ω, as shown in Fig. 15(b), the lower output voltage v_z reaches a required high phase shift φ_r (about 57°). Fig. 15(c)–(f) shows the phase-shift angle φ_r under a load resistance of $15, 20, 30$, and $40\,\Omega$, respectively. It can be seen that the phase-shift angle φ_r will gradually increase to about 67° when the load resistance changes to $40\,\Omega$. This result illustrates that the output voltage

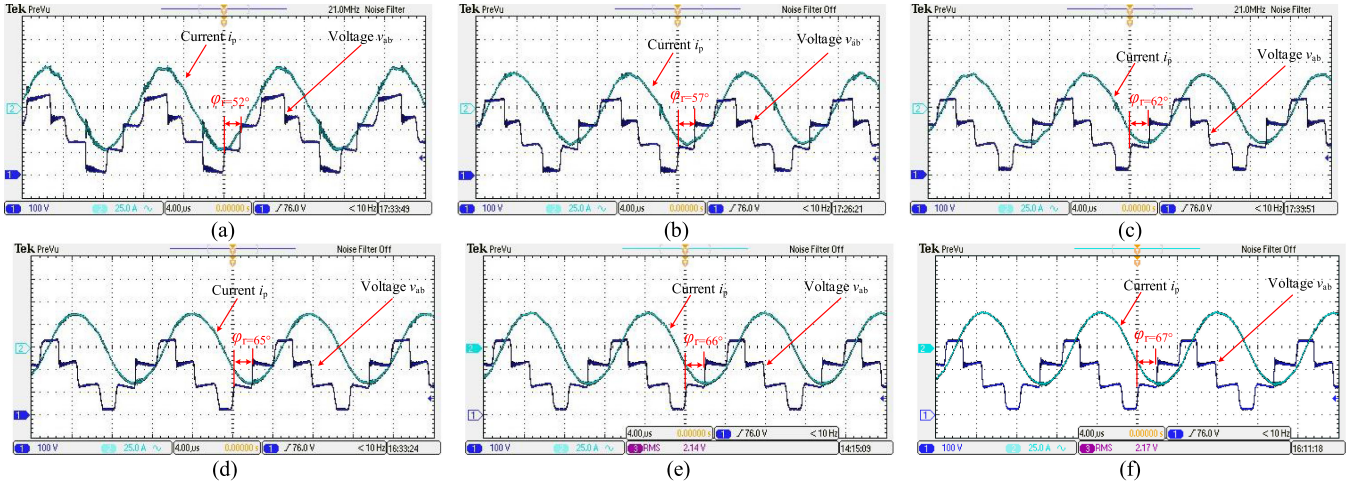

Fig. 15. Output voltage and current waveforms of the inverter under a reference of 125 V at different loads. (a) Rb = 5 Ω. (b) Rb = 10 Ω. (c) Rb = 15 Ω. (d) Rb = 20 Ω. (e) Rb = 30 Ω. (f) Rb = 40 Ω.

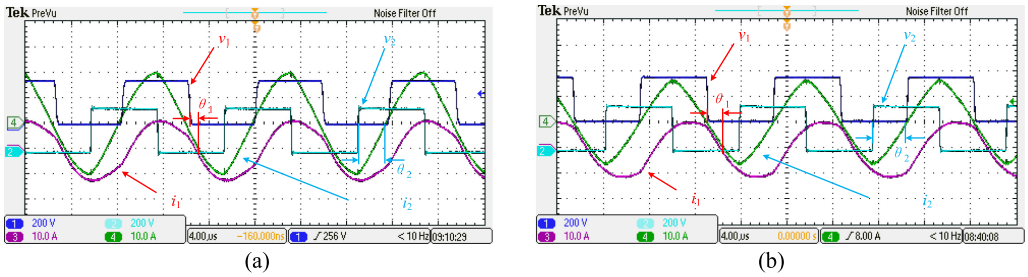

Fig. 16. Output voltage and current of phases where channels 1 and 3 are for the second phase while 2 and 4 for the third phase. (a) For 5 Ω load resistance. (b) For 10 Ω load resistance.

can be controlled by changing the phase angle among three phases at a constant operating frequency.

Experimental waveforms of the voltage and current of each phase under 15 cm misalignment were captured and shown in Fig. 16 to verify the ZVS conditions. Because the impedance angle of the first phase is always higher than those of other phases, only the second and the third phases were measured in the experiment. Again, one can see that the impedance angles increase consistent with the trend of Fig. 10, namely, the impedance angles for load resistance higher than 10 Ω will be higher than that of 10 Ω. This also proves that ZVS operation can be obtained.

VI. Conclusion

In this paper, a multiphase phase-controlled inverter is used for S-S compensated IPT system as a supply instead of the traditional class-D full-bridge or half-bridge resonant inverter. The charging voltage is regulated by adjusting the phase angle among phases under a fixed frequency. A dynamic model including the phase-controlled inverter and entail IPT system is developed and linearized to analyze the dynamic characteristics. For the high order of the model, a balanced model reduction method is used to remove the fast modes that are outside the desired system bandwidth and insignificant to controller design. Considering that the control feedback loop in the experiment is set up by the wireless modules, a few unit delays are added to the discrete model by using Pade transform method. Also, the discrete domain analysis of the reduced model is conducted, which is more suitable for the digital control. The phase margin, amplitude margin, settling time, and overshoot are all considered as the requirement performances in the development of the controller. This is especially useful when the system is required to be tightly designed in terms of its preset settling time or overshoot. In the experiment, a 6.5 kW physical IPT system with the designed digital PI controller is constructed. The recorded response curves and steady-state waveforms convincingly demonstrate that the charging voltage can be maintained at a constant in the charging process with good stability and dynamic performance.

Appendix

Variables in (12) and (14)

$$A_1 = L_p / \left(L_p L_s - M^2\right)$$

$$A_2 = L_s / \left(L_p L_s - M^2\right)$$

$$A_3 = M / \left(L_p L_s - M^2\right)$$

$$A_4 = 4V_o I_{sq}^2 / \left(\pi |i_s|^3\right) + R_s$$

$$A_5 = 4V_o I_{sd}^2 / \left(\pi |i_s|^3\right) + R_s$$

$$A_6 = 4I_{sd}/\left(\pi\left|i_s\right|\right)$$
$$A_7 = 4I_{sq}/\left(\pi\left|i_s\right|\right)$$
$$A_8 = 4V_o I_{sd} I_{sq}/\left(\pi|i_s|^3\right)$$
$$A_9 = \frac{2V_I}{N\pi} A_{10} \sin^{-2}\varphi_n \cdot \frac{\pi}{180}$$
$$A_{10} = \cos\varphi_n \sin\frac{\varphi_n}{N} - \frac{1}{N}\sin\varphi_n \cos\frac{\varphi_n}{N}$$
$$A_{11} = 4V_o/\left(\pi\sqrt{I_{sd}^2 + I_{sq}^2}\right)$$

REFERENCES

[1] R. Mai, Y. Chen, Y. Zhang, N. Yang, G. Cao, and Z. He, "Optimization of the passive components for an S-LCC topology-based WPT system for charging massive electric bicycles," *IEEE Trans. Ind. Electron.*, vol. 65, no. 7, pp. 5497–5508, Jul. 2018.

[2] F. Liu, Y. Yang, Z. Ding, X. Chen, and R. M. Kennel, "A multifrequency superposition methodology to achieve high efficiency and targeted power distribution for a multiload MCR WPT system," *IEEE Trans. Power Electron.*, vol. 33, no. 10, pp. 9005–9016, Oct. 2018.

[3] Y. Yao, Y. Wang, X. Liu, F. Lin, and D. Xu, "A novel parameter tuning method for a double-sided LCL compensated WPT system with better comprehensive performance," *IEEE Trans. Power Electron.*, vol. 33, no. 10, pp. 8525–8536, Oct. 2018.

[4] Q. Deng, J. Liu, D. Czarkowski, W. Hu, and H. Zhou, "An inductive power transfer system supplied by a multiphase parallel inverter," *IEEE Trans. Ind. Electron.*, vol. 64, no. 9, pp. 7039–7048, Mar. 2017.

[5] Y. Liu, R. Mai, D. Liu, Y. Li, and Z. He, "Efficiency optimization for wireless dynamic charging system with overlapped DD coil arrays," *IEEE Trans. Power Electron.*, vol. 33, no. 4, pp. 2832–2846, Apr. 2018.

[6] G. Buja, M. Bertoluzzo, and K. N. Mude, "Design and experimentation of WPT charger for electric city car," *IEEE Trans. Ind. Electron.*, vol. 62, no. 12, pp. 7436–7447, Dec. 2015.

[7] Z. Nie and Y. Yang, "A model independent scheme of adaptive focusing for wireless powering to in-body shifting medical device," *IEEE Trans. Antennas Propag.*, vol. 66, no. 3, pp. 1497–1506, Mar. 2018.

[8] P. Chen, H. Yang, R. Luo, and B. Zhao, "A tissue-channel transcutaneous power transfer technique for implantable devices," *IEEE Trans. Power Electron.*, vol. 33, no. 11, pp. 9753–9761, Nov. 2018.

[9] J. Park *et al.*, "A resonant reactive shielding for planar wireless power transfer system in smartphone application," *IEEE Trans. Electromagn. Compat.*, vol. 59, no. 2, pp. 695–703, Apr. 2017.

[10] P. Si, A. P. Hu, S. Malpas, and D. Budgett, "A frequency control method for regulating wireless power to implantable devices," *IEEE Trans. Biomed. Circuits Syst.*, vol. 2, no. 1, pp. 22–29, Mar. 2008.

[11] S. Zheng and D. Czarkowski, "Modeling and digital control of a phase-controlled series-parallel resonant converter," *IEEE Trans. Ind. Electron.*, vol. 54, no. 2, pp. 707–715, Apr. 2007.

[12] W. Shi, J. Deng, Z. Wang, and X. Cheng, "The start-up dynamic analysis and one cycle control-PD control combined strategy for primary-side controlled wireless power transfer system," *IEEE Access*, vol. 6, pp. 14439–14450, 2018.

[13] J. M. Miller, O. C. Onar, and M. Chinthavali, "Primary-Side power flow control of wireless power transfer for electric vehicle charging," *IEEE J. Emerg. Sel. Topics Power Electron.*, vol. 3, no. 1, pp. 147–162, Mar. 2015.

[14] S. Samanta and A. K. Rathore, "Small-Signal modeling and closed-loop control of a parallel–series/series resonant converter for wireless inductive power transfer," *IEEE Trans. Ind. Electron.*, vol. 66, no. 1, pp. 172–182, Jan. 2019.

[15] A. K. Swain, S. Devarakonda, and U. K. Madawala, "Modeling, sensitivity analysis, and controller synthesis of multipickup bidirectional inductive power transfer systems," *IEEE Trans. Ind. Electron.*, vol. 10, no. 2, pp. 1372–1380, May 2014.

[16] F. Liu, K. Chen, Z. Zhao, K. Li, and L. Yuan, "Transmitter-Side control of both the CC and CV modes for the wireless EV charging system with the weak communication," *IEEE J. Emerg. Sel. Topics Power Electron.*, vol. 6, no. 2, pp. 955–965, Jun. 2018.

[17] K. Aditya and S. S. Williamson, "Comparative study on primary side control strategies for series-series compensated inductive power transfer system," in *Proc. IEEE 25th Int. Symp. Ind. Electron.*, Santa Clara, CA, USA, 2016, pp. 811–816.

[18] K. Aditya and S. Williamson, "Linearization and control of series-series compensated inductive power transfer system based on extended describing function concept," *Energies*, vol. 9, no. 11, pp. 1–16, Nov. 2016.

[19] A. K. Swain, M. J. Neath, U. K. Madawala, and D. J. Thrimawithana, "A dynamic multivariable state-space model for bidirectional inductive power transfer systems," *IEEE Trans. Power Electron.*, vol. 27, no. 11, pp. 4772–4780, Nov. 2012.

[20] K. Hata, T. Imura, and Y. Hori, "Dynamic wireless power transfer system for electric vehicles to simplify ground facilities - power control and efficiency maximization on the secondary side," in *Proc. IEEE Appl. Power Electron. Conf. Expo.*, Long Beach, CA, USA, 2016, pp. 1731–1736.

[21] Y. Yang, W. Zhong, S. Kiratipongvoot, S. C. Tan, and S. Y. R. Hui, "Dynamic improvement of series–series compensated wireless power transfer systems using discrete sliding mode control," *IEEE Trans. Power Electron.*, vol. 33, no. 7, pp. 6351–6360, Jul. 2018.

[22] H. H. Wu, A. Gilchrist, K. D. Sealy, and D. Bronson, "A high efficiency 5 kW inductive charger for EVs using dual side control," *IEEE Tran. Ind. Inform.*, vol. 8, no. 3, pp. 585–595, Aug. 2012.

[23] C. Song *et al.*, "EMI reduction methods in wireless power transfer system for drone electrical charger using tightly coupled three-phase resonant magnetic field," *IEEE Trans. Ind. Electron.*, vol. 65, no. 9, pp. 6839–6849, Sep. 2018.

[24] M. K. Kazimierczuk and M. Jutty, "Fixed-Frequency phase-controlled full-bridge resonant converter with a series load," *IEEE Trans. Power Electron.*, vol. PE-10, no. 1, pp. 9–18, Jan. 1995.

[25] M. K. Kazimierczuk, "Synthesis of phase-modulated dc/ac inverters and dc/dc converters," *Inst. Elect. Eng. Proc. B-Elect. Power Appl.*, vol. 139, pp. 387–394, Jul. 1992.

[26] D. Czarkowski and M. K. Kazimierczuk, "Single-Capacitor phase-controlled series resonant converter," *IEEE Trans. Circuits Syst.*, vol. CAS-40, no. 6, pp. 383–391, Jun. 1993.

[27] D. Czarkowski and M. K. Kazimierczuk, "Phase-controlled series-parallel resonant converter," *IEEE Trans. Power Electron.*, vol. PE-8, no. 3, pp. 309–319, Jul. 1993.

[28] M. K. Kazimierczuk and M. K. Jutty, "Phase-Modulated series-parallel resonant converter with series load," *Inst. Elect. Eng. Proc. B-Elect. Power Appl.*, vol. 140, pp. 297–306, Sep. 1993.

[29] M. K. Kazimierczuk, D. Czarkowski, and N. Thirunarayan, "A new phase-controlled parallel resonant converter," *IEEE Trans. Ind. Electron.*, vol. IE-40, no. 6, pp. 542–552, Dec. 1993.

[30] Z. U. Zahid, Z. Dalala, and J. S. J. Lai, "Small-signal modeling of series-series compensated induction power transfer system," in *Proc. IEEE Appl. Power Electron. Conf. Expo.*, Fort Worth, TX, USA, 2014, pp. 2847–2853.

[31] Z. U. Zahid *et al.*, "Modeling and control of series–series compensated inductive power transfer system," *IEEE J. Emerg. Sel. Topics Power Electron.*, vol. 3, no. 1, pp. 111–123, Mar. 2015.

[32] K. Aditya and S. S. Williamson, "Advanced controller design for a series-series compensated inductive power transfer charging infrastructure using asymmetrical clamped mode control," in *Proc. IEEE Appl. Power Electron. Conf. Expo.*, Charlotte, NC, USA, 2015, pp. 2718–2724.

[33] Q. Deng, J. Liu, D. Czarkowski, M. Bojarski, E. Asa, and F. de Leon, "Design of a wireless charging system with a phase-controlled inverter under varying parameters," *IET Power Electron.*, vol. 9, no. 13, pp. 2461–2470, Oct. 2016.

[34] M. Bojarski, D. Czarkowski, F. de Leon, Q. Deng, M. K. Kazimierczuk, and H. Sekiya, "Multiphase resonant inverters with common resonant circuit," in *Proc. IEEE Int. Symp. Circuit Syst.*, Melbourne, VIC, Australia, 2014, pp. 2445–2448.

[35] M. Bojarski, E. Asa, K. Colak, and D. Czarkowski, "Analysis and control of multiphase inductively coupled resonant converter for wireless electric vehicle charger applications," *IEEE Trans. Transp. Electrific.*, vol. 3, no. 2, pp. 312–320, Jun. 2017.

[36] K. Aditya and S. S. Williamson, "A review of optimal conditions for achieving maximum power output and maximum efficiency for a series–series resonant inductive link," *IEEE Trans. Transp. Electrific.*, vol. 3, no. 2, pp. 303–311, Jun. 2017.

[37] A. Khaligh and Z. Li, "Battery, ultracapacitor, fuel cell, and hybrid energy storage systems for electric, hybrid electric, fuel cell, and plug-in hybrid electric vehicles: State of the art," *IEEE Trans. Veh. Technol.*, vol. 59, no. 6, pp. 2806–2814, Jul. 2010.

Qijun Deng received the B.S. and M.Sc. degrees in mechanical engineering and the Ph.D. degree in computer application technology from Wuhan University, Wuhan, China, in 1999, 2002, and 2005, respectively.

In June 2005, he joined the Department of Automation, Wuhan University, where he is currently an Associate Professor. From 2013 to 2014, he was a Visiting Scholar with the New York University Tandon School of Engineering.

His research interests include wireless power transfer, distribution automation, and electrical power informatics.

Ziyi Wang received the B.S. degree in automation from Wuhan University, Wuhan, China, in 2019. She is currently working toward the Ph.D. degree with the Department of Mechanical and Automation Engineering, The Chinese University of Hong Kong, Hong Kong.

Her current research interests include medical robotics and visual servo.

Cheng Chen (S'18) received the M.S. degree in control engineering and the Ph.D. degree in mechatronic engineering from Wuhan University, Wuhan, China, in 2015 and 2019, respectively.

In 2019, he joined the School of Electrical Engineering, PLA Naval University of Engineering, Wuhan, where he is currently a Lecturer. His current research interests include system modeling, nonlinear control, and wireless power transfer.

Dariusz Czarkowski (M'97) received the M.Sc. degree in electronics from the AGH University of Science and Technology, Krakow, Poland, in 1989, the M.Sc. degree in electrical engineering from Wright State University, Dayton, OH, USA, in 1993, and the Ph.D. degree in electrical engineering from the University of Florida, Gainesville, FL, USA, in 1996.

In 1996, he joined New York University Tandon School of Engineering, Brooklyn, NY, USA, where he is currently an Associate Professor in electrical and computer engineering. He is a Co-Author of the book *Resonant Power Converters* (Wiley-IEEE Interscience, 2011). His current research interests include power electronics and power distribution systems.

Dr. Czarkowski was an Associate Editor for the IEEE TRANSACTIONS ON CIRCUIT AND SYSTEMS.

Marian K. Kazimierczuk (M'91–SM'91–F'04) received the M.S., Ph.D., and D.Sci. degrees in electronics engineering from the Warsaw University of Tecbnology, Warsaw, Poland, in 1971, 1978, and 1984, respectively.

He was a Teaching and Research Assistant with the Department of Electronics, Institute of Radio Electronics, Warsaw University of Technology, from 1972 to 1978, where he was an Assistant Professor from 1978 to 1984. In 1984, he was a Project Engineer with Design Automation, Inc., Lexington, MA, USA. In 1984/1985, he was a Visiting Professor with the Department of Electrical and Computer Engineering, Virginia Polytechnic Institute and State University, Blacksburg, VA, USA. Since 1985, he has been with the Department of Electrical Engineering, Wright State University, Dayton, OH, USA, where he is currently a Distinguished Professor. His research interests include high-frequency high-efficiency switch-mode tuned power amplifiers, resonant and PWM dc/dc power converters, dc/ac inverters, high-frequency rectifiers, electronic ballasts, power factor correction, modeling and control of converters, high-frequency magnetics, wireless power transfer, gate drivers, and power semiconductor devices. He is the Author of six books and three solutions manuals on *Pulse-Width Modulated DC-DC Power Converters,* 2nd Ed (John Wiley & Sons, 2015*), RF Power Amplifiers,* 2nd Ed (John Wiley & Sons, 2015), and *High-Frequency Magnetic Components,* 2nd Ed (John Wiley & Sons, 2014). He is the Co-Author of the books *Resonant Power Converters*, 2nd Ed (IEEE Press/John Wiley& Sons, 2011), *Solutions for Resonant Power Converters* (John Wiley & Sons, 2005), *Electronic Devices, A Design Approach* (Prentice Hall, 2004), and *Lab Manual* (Prentice Hall, 2011). He has authored or coauthored more than 210 journal papers and more than 260 conference papers. More than 180 papers have appeared in IEEE transactions and journals. He is also the holder of eight patents.

Prof. Kazimierczuk is the recipient of the IEEE Harrell V. Noble Award for his contributions to the fields of aerospace, industrial, and power electronics in 1991. In 2010, he was named National Professor of Technical Sciences by Poland President Lech Kaczynski. He was an Associate Editor for the IEEE TRANSACTIONS ON CIRCUITS AND SYSTEMS-I: REGULAR PAPERS and an Associate Editor for the *Journal of Circuits, Systems, and Computers*. He is an Associate Editor for the IEEE TRANSACTIONS ON INDUSTRIAL ELECTRONICS, the *International Journal of Circuit Theory and Applications*, and the *IET Circuits, Devices and Systems*. He was a member of the Superconductivity Committee of the IEEE Power Electronics Society. He was a Chair of the IEEE Circuits and Systems Society Technical Committee of Power Systems and Power Electronics Circuits in 2001 and 2002. He is a member of Tau Beta Pi. He was the recipient of the Presidential Awards in Research, Teaching, and Professional Service as well as the Trustee's Award from Wright State University. He has won the Best Paper Award from *IET Power Electronics* in 2012.

Hong Zhou (M'18) received the B.S. degree in automation from Central South University of Technology (now Central South University), Changsha, China, in 1982, the M.Sc. degree in control theory and applications from Chongqing University, Chongqing, China, in 1988, and the Ph.D. degree in mechanical engineering from Wuhan University, Wuhan, China, in 2006.

He was an Assistant Engineer with Changshou Power Plant, Chongqing, from 1982 to 1985. Since 1992, he has been with the Wuhan University of Hydraulic and Electrical Engineering (now a part of Wuhan University), Wuhan. He was the Head of the Department of Automation, Wuhan University, from 2002 to 2006 and has been a Professor with the Department since 2000. His main research interests include wireless power transfer, smart grids, and networked control systems.

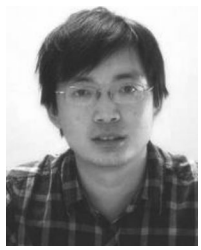

Wenshan Hu (M'18) received the B.S. and M.Sc. degrees in control theory and applications from Wuhan University, Wuhan, China, in 2002 and 2004, respectively, and the Ph.D. degree in control engineering from the University of Glamorgan, Pontypridd, U.K., in 2008.

He is currently a Professor with the Department of Automation, Wuhan University. His research interests include network-based control laboratories and wireless power transfer.